E3S Web of Conferences **730**, 02011 (2026)
Soft Soils 2026
https://doi.org/10.1051/e3sconf/202673002011

A numerical study addressing CPTu inversion in organic soils containing gas

Arthur Halleux[1*], *Katia* Boschi [1], *Luca* Flessati [2], and *Cristina* Jommi [1,2]

[1] Department of Civil and Environmental Engineering, Politecnico di Milano, Milano, Italy
[2] Department of Geoscience and Engineering, Delft University of Technology, Delft, The Netherlands

Abstract. Soft organic soils often contain gas pockets generated by the chemical decomposition of organic matter. The gas content fluctuates seasonally with temperature and barometric pressure, can alter the soil mechanical response and complicates the interpretation of cone penetration test (CPT) results. The influence of gas on CPT response remains poorly understood, resulting in a critical gap in knowledge that can potentially lead to either unsafe or overly conservative engineering design. This study starts investigating the role of gas content on CPT results, using a numerical approach based on a coupled hydro-mechanical particle finite element formulation. In the analysis, the gas volume fraction is incorporated by adjusting the compressibility of the fluid that saturates the pore space. The findings demonstrate how accounting for gas content enables more accurate interpretation of CPT results and more reliable estimation of shear strength. A strategy for simultaneously estimating gas content and undrained shear strength in organic gassy soils using CPT data is proposed. The study further suggests that both the gas volume fraction and the cone factor can be theoretically inferred from the spatial distribution of pore pressure, providing a practical means to enhance design safety and cost-effectiveness in soft soil engineering.

1 Introduction

Cone penetration tests with pore pressure measurement (CPTu) are widely used in the practice to determine the undrained shear strength profile of soft soils [1]. The strength is estimated from the net cone tip resistance using a cone factor that is either determined through experience or calibrated based on laboratory test results [2-4]. For organic clays, cone factors reported in the literature range from 8.6 to 15.3 [5]. In the absence of specific calibration, this uncertainty can result in either over- or under-estimation of undrained shear strength, which compromises the reliability of CPT-based design and assessment.

Differences in cone factors between various organic clays can be attributed to their different compressibility and hydraulic conductivity in the pre-failure deformation stages [2-4]. However, the presence of gas from organic matter decomposition is also expected to affect the hydro-mechanical response of organic soils, in turn influencing the cone factor to be used in the interpretation of the data. Even if the influence of volumetric gas fraction on the undrained response of soft soils has been investigated in the past [6-9], only a few works have addressed the evidence and the consequences of a gas volume fraction on CPTu readings [10-12]. The relationship between gas volume fraction, undrained shear strength and CPTu readings on organic soft soils has not yet been investigated.

This contribution, which is part of a wider study aimed at improving current approaches for interpreting CPTu in organic clays [13,14], includes (i) the proposal of a theoretical approach for determining the variation of undrained shear strength with realistic gas volume fractions, (ii) a numerical study of the influence of gas on CPTu results, and (iii) a discussion on how to account for gas in the interpretation of these results. The study shows how to estimate the gas volume fraction using CPTu measurements and how to derive the cone factor value to infer the undrained shear strength.

2 Theoretical approach

Finite kinematics coupled hydro-mechanical numerical analyses are performed [15,16]. The soil is assumed to be saturated by an equivalent compressible liquid, whose compressibility is estimated based on the gas volume fraction and remains constant. It is worthwhile mentioning that the study is focussed on gas fractions that do not overpass the gas entry value of the soil, for which the standard framework for saturated soils holds.

The soil mechanical behaviour is modelled through the strain hardening elastic-plastic constitutive relationship CASM [17], with model parameters calibrated on the results of laboratory tests performed on organic clay samples retrieved at Leendert de Boerspolder [18,19]. The soil hydraulic response follows Darcy's law with an isotropic hydraulic conductivity $k_{hyd} = 5.10^{-8}$ m/s. The full set of parameters adopted in the simulation is reported in Table 1.

* Corresponding author: arthur.halleux@polimi.it

Table 1. Initial Poisson's ratio ν_0, virgin isotropic void ratio N at $p'_r = 1$ kPa, reloading index κ, virgin compression index λ, slope of the Critical State Line (CSL) in triaxial compression M in (p', q) plane, yield surface shape parameters n and r and plastic potential shape parameter m.

ν_0	N	κ	λ	M	n	r	m
0.35	4.2	0.023	0.218	1.42	2	2	2

The soil is assumed to be saturated by an equivalent compressible liquid, mimicking the presence of gas inclusions in the pore water. The equivalent water–gas mixture is characterised by a compressibility β_f:

$$\beta_f = \phi \cdot \beta_g + (1 - \phi) \cdot \beta_w \tag{1}$$

where β_g, β_w and ϕ are the gas compressibility, the pure water compressibility and the gas volume fraction, respectively.

The β_f values used in the analysis (Table 2) are calculated according to [20], considering: (i) pure water compressibility equal to $\beta_w = 4.5 \cdot 10^{-7}$ kPa^{-1}; (ii) a volumetric percentage of methane between 0% and 10% (% CH4); (iii) a water-methane interfacial tension of $5 \cdot 10^{-5}$ kN/m [21]; (iv) initial pore pressure $u_0 = 30$ kPa and initial void ratio $e_0 = 3.35$; (v) dry density ρ_d and specific surface S of the organic clay samples retrieved at Leendert de Boerspolder (ρ_d = 1.35 g/cm^3 and S ranging between 0.1 and 20 m^2/g as a function of clay content).

Table 2. β_f values as a function of S and % CH4.

β_f [kPa^{-1}]	S [m^2/g]	% CH_4 [%]
$4.5 \cdot 10^{-7}$	-	0
$1 \cdot 10^{-4}$	3	5
$2 \cdot 10^{-4}$	2	7
$1 \cdot 10^{-3}$	0.1	10

2.1 Analytical derivation of undrained shear strength, S_u^*

In the case of a soil saturated with a compressible fluid, undrained conditions are not associated with zero volumetric strains. The undrained shear strength S_u^* is expected to be different from the standard undrained shear strength value S_u when water is assumed incompressible. To derive an analytical expression for S_u^* under triaxial compression conditions, the CASM constitutive law is integrated over the stress path by imposing:

$$d\varepsilon_{vol}^{el} + d\varepsilon_{vol}^{pl} = \frac{e}{1+e}\,\beta_f \cdot du \tag{2}$$

where d stands for increment, ε_{vol}^{el} and ε_{vol}^{pl} are the elastic and plastic volumetric strains, respectively, e is the void ratio and u indicates the pore water pressure.

Under the simplifying assumption of small displacements and strains ($e = e_0$), the elastic response over the triaxial compression effective stress path is given by:

$$dq = 3 \cdot \left[1 + \frac{\kappa}{e_0\, \beta_f\, p'}\right] dp' \tag{3}$$

where p' is the effective isotropic stress and q is the deviatoric stress.

The equation provides insight into how fluid compressibility influences the evolution of the integrated stress path. To further highlight this, a ratio between the soil and fluid compressibility is introduced:

$$R_{el}(p') = \frac{\kappa}{e\, \beta_f\, p'} \tag{4}$$

which holds until the soil skeleton remains in the elastic range. It can be appreciated that for:

- $\beta_f \to 0 : R_{el}$ goes to infinity. The elastic path for the undrained case with full saturation, that is a vertical line in the (p', q) plane, is recovered.
- $\beta_f \to \infty : R_{el}$ goes to 0. The fluid mixture is unable to withstand any stress, and the classical "drained" stress path is obtained: $dq = 3dp'$.

When the yield surface is reached, the compressibility ratio changes to:

$$R_{ep}(p') = \frac{\lambda}{e\, \beta_f\, p'} \tag{5}$$

and the elastic-plastic stress path can be written as:

$$\begin{gathered}\left[\frac{1 + R_{ep}(p')}{R_{ep}(p')} - \Lambda \frac{n \ln(r)}{M^n} \cdot \left(\frac{q}{p'}\right)^n\right] dp' = [\ldots] \\ [\ldots] = \left[\frac{1}{3R_{ep}(p')} - \Lambda \frac{n \ln(r)}{M^n} \left(\frac{q}{p'}\right)^{n-1}\right] dq\end{gathered} \tag{6}$$

where $\Lambda = (\lambda - \kappa) / \lambda$.

Numerical integration of Equation 6 from the yield condition $(p', q) = (p'_y, q_y)$ (the values of p' and q at yielding) up to critical state, corresponding to $q_{CS} = M \cdot p'_{cs}$ and $S_u^* = 0.5 \cdot q_{cs}$ allows to determine the soil undrained strength. To get the yield condition p'_y and q_y, Equation 2 is analytically integrated from the initial values of p' and q (p'_0 and q_0) and combined with the CASM yield surface:

$$f = \left(\frac{q}{p'M}\right)^n + \frac{1}{\ln r} \ln \frac{p'}{p_0^*} \tag{7}$$

The resulting stress paths are illustrated in Fig. 1 for $OCR = 1.1$ and $OCR = 4$. In Fig. 2, the ratio S_u^*/S_u is reported as a function of the initial elastoplastic compressibility ratio:

$$R_{ep}(p'_0) = \frac{\lambda}{e\, \beta_f\, p'_0} \tag{8}$$

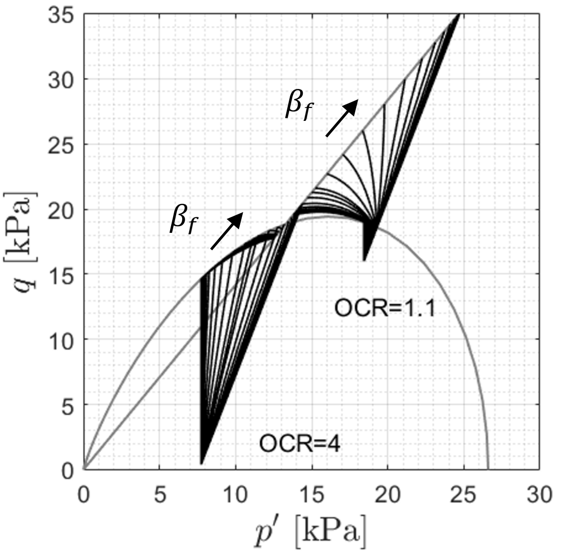

Fig. 1. Effective stress paths (ESP) for $OCR = 1.1$ and $OCR = 4$. The ending point on the CSL corresponds to S_u^*.

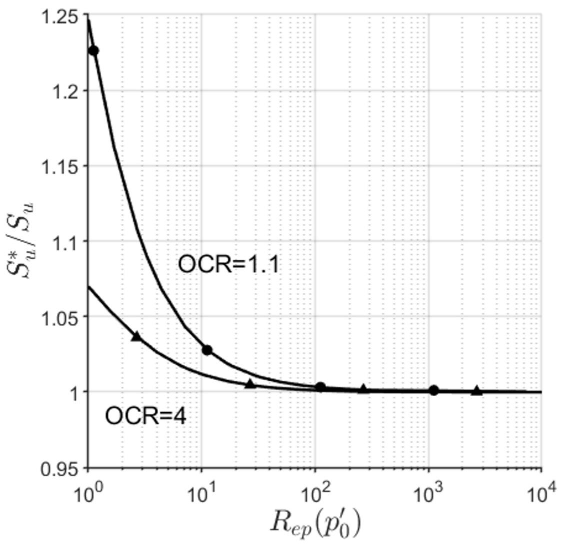

Fig. 2. Evolution of S_u^*/S_u with $R_{ep}(p_0')$. Data points correspond to β_f values listed in Table 2 (circles for OCR =1.1, triangles for OCR = 4).

The two different curves in Fig. 2 are obtained by imposing an initial anisotropic effective stress state, ruled by the at-rest lateral earth pressure coefficient $K_0 = (1 - sin\,\phi')\,OCR^{0.5}$, where ϕ' is the critical state friction angle (uniquely related to M) and OCR the over-consolidation ratio of the soil element.

The initial value of the hardening variable p_0^* of Equation 7 depends on both OCR and $K_0^* = (1 - sin\,\phi')$. According to the employed constitutive model, for the considered initial states, S_u^* is always larger than S_u. Their ratio increases at decreasing relative fluid-soil stiffness ratio and decreases at increasing OCR. The influence of the relative fluid-stiffness ratio on the strength ratio S_u^*/S_u becomes negligible at values above $1e2$.

3 Numerical simulation of CPTu

CPTu are reproduced with G-PFEM, the Geotechnical code based on Particle Finite Element Method developed at CIMNE-UPC [22-23] and implemented in Kratos Multiphysics [24]. The code features (i) fully coupled hydro-mechanical formulation, (ii) finite kinematics, (iii) continuous refinement of the finite element mesh where larger irreversible strains develop, and (iv) a non-local regularization technique [25].

3.1 Numerical model

The CPTu tests are simulated by assuming an axisymmetric geometry. The cone is modelled with a radius $R = 17.84$ mm, an apex angle of $60°$ and a cylindrical friction sleeve height of 134 mm. At the cone-soil interface, only compressive normal forces are allowed, and the contact exhibits elastic-plastic behaviour in the tangential direction, with a chosen interface friction angle $\delta = 15°$. The cone is initially positioned at a depth of $17R$ and then pushed at a constant velocity $v = 2$ cm/s.

The computational domain, large enough to avoid any boundary effect [16], is $45R$ wide and $60R$ deep. Boundary conditions include: (i) nil normal displacements at the bottom and along vertical boundaries, (ii) uniform surcharge at the top, equal to the initial total vertical stress $\sigma_{v0} = \sigma'_{v0} + u_0$ (where σ'_{v0} is the initial vertical effective stress), (iii) no horizontal seepage across vertical boundaries and (iv) constant pore pressure $u = u_0$ over the top and bottom boundaries.

An initial uniform stress state is imposed, which replicates the initial conditions of the samples tested at the Leendert de Boerspolder site. The initial pore pressure, u_0, is set to 30 kPa, and two different $\sigma'_{v,0}$ and OCR values are considered. In the first case, $\sigma'_{v,0} = 29$ kPa and $OCR = 1.1$, whereas in the second one $\sigma'_{v,0} = 8$ kPa and $OCR = 4$, replicating the information to obtained from onsite data.

The two combinations turn out to have nearly identical maximum vertical effective stress, equal to $\sigma'_{v,max} = \sigma'_{v,0} \cdot OCR = 32$ kPa. The initial horizontal effective stress σ'_{h0} is imposed through K_0, and the initial p_0^* value is imposed by considering $\sigma'_{v,max}$ and a maximum horizontal effective stress $\sigma'_{h,max} = K_0^* \cdot \sigma'_{v,max}$. The β_f values used in the numerical simulations are reported in Table 2.

3.2 Numerical results

All the results presented hereafter are the asymptotic values reached after $10R$ of penetration (negligibly affected by the upper boundary [16]). The fluid compressibility influences both the cone tip resistance q_t and the excess pore water pressure Δu. The numerical results are reported in Fig. 3 to Fig. 6.

In the first one, the results are plotted as variation of $q_{net}/\sigma'_{v0} = (q_t - \sigma_v)/\sigma'_{v0}$ ratio with S_u^*/σ'_{v0}, where S_u^* is the corresponding value calculated by integrating Equation 6. From a quantitative perspective, the effect

https://doi.org/10.1051/e3sconf/202673002011

of β_f on q_{net} is significantly larger than its effect on S_u^*, implying that the cone factor $N_{kt}^* = q_{net} / S_u^*$ also strongly depends on β_f. The straight lines representing the lower (10.1) and the upper bound (16.1) found for N_{kt}^* are also plotted in Fig. 3. These values are in good agreement with the $N_{kt} = q_{net} / S_u$ range obtained by [5], suggesting that the presence of gas can justify at least part of the very large dispersion of cone factor values for organic clays.

In Fig. 4, the variation of N_{kt}^* with the relative fluid-soil skeleton stiffness is illustrated. The plot shows that N_{kt}^* decreases significantly until the fluid-soil skeleton compressibility ratio reaches a value of $1e^2$. It is worth noting that the values plotted in the figure also depend on the parameters chosen to model the reference material. However, the trend will hold irrespective of the specific type of organic soil.

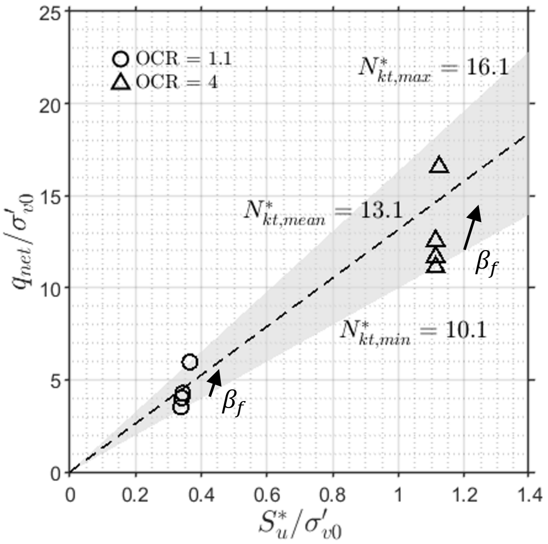

Fig. 3. Evolution of q_{net}/σ'_{v0} with S_u^*/σ'_{v0}.

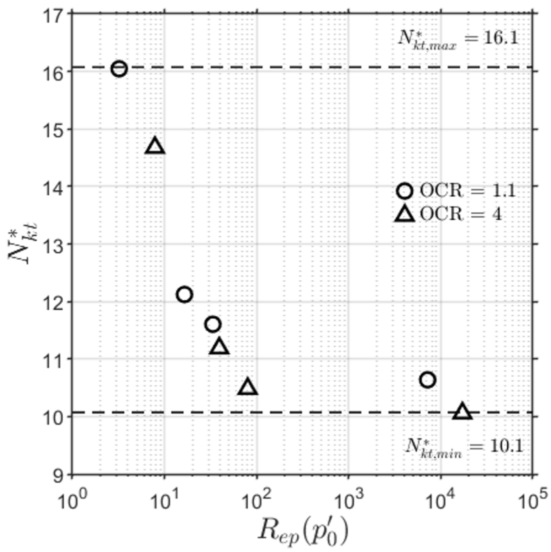

Fig. 4. Evolution of N_{kt}^* with $R_{ep}(p'_0)$.

The contours of Δu, each normalised with respect to its maximum (Δu_{max}), are shown in four different cases varying both OCR and β_f in Fig. 5 and Fig. 6. On the left-hand side of the figure the incompressible fluid case is reported, while the results obtained adopting a fluid compressibility of $\beta_f = 10^{-3}$ kPa^{-1} are plotted on the right one. Fig. 5 shows the results for the normally consolidated case ($OCR \approx 1$) and Fig. 6 the ones for the overconsolidated case ($OCR = 4$).

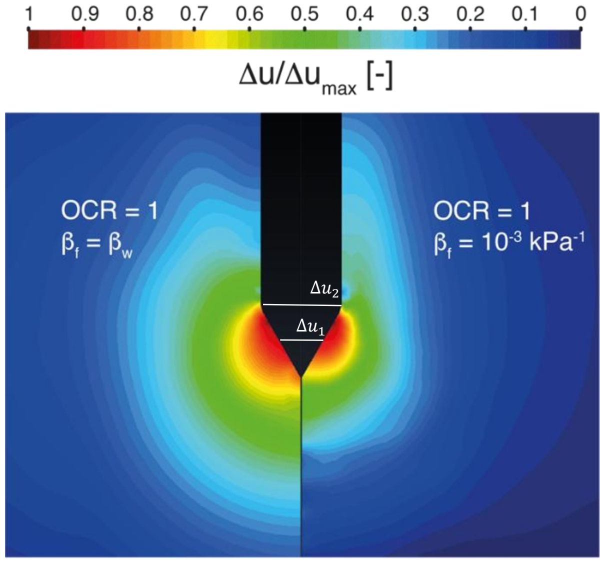

Fig. 5. Contours of normalised excess pore pressure at the cone tip corresponding to a penetration $z = 10R$ for the normally consolidated case.

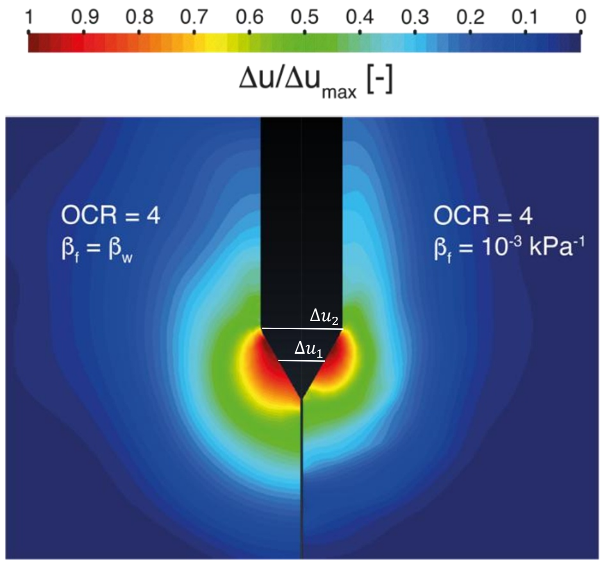

Fig. 6. Contours of normalized excess pore pressure at the cone tip corresponding to a penetration $z = 10R$ for $OCR = 4$.

For both OCR values, in the absence of gas content ($\beta_f = \beta_w$), the increase in Δu covers a wide region around the cone tip. Conversely, for $\beta_f = 10^{-3}$ kPa^{-1}, the Δu distribution mainly localises beneath the cone tip midface. The Δu distribution close to the cone tip appears to be significantly more influenced by β_f than OCR. From a practical perspective, this suggests that pore pressure measures taken at different locations of the cone tip can be used as an indirect measure of the relative fluid-soil stiffness ratio, which can then be used as a proxy for the gas volume fraction for the soil. For instance, considering the standard positions of pore water pressure measurements Δu_1 and Δu_2, at cone tip midface and shoulder, respectively, the $\Delta u_1/\Delta u_2$ ratio can be related to $R_{ep}(p'_0)$ as shown in Fig. 7.

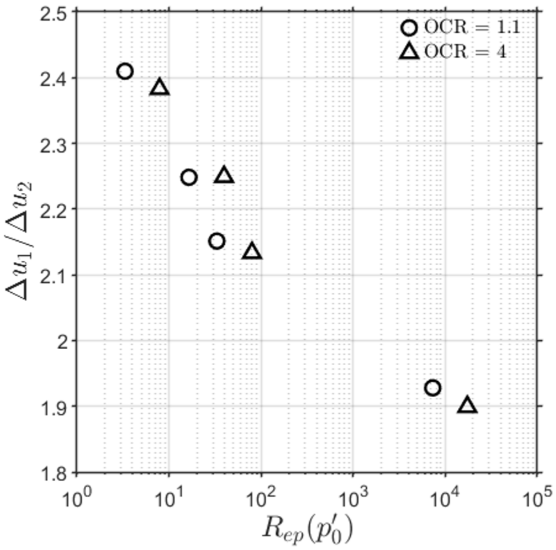

Fig. 7. Evolution of $\Delta u_1/\Delta u_2$ ratio with $R_{ep}(p'_0)$.

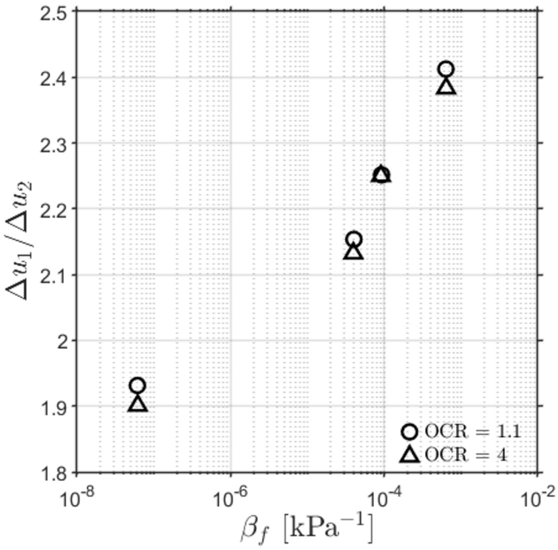

Fig. 8. Evolution of $\Delta u_1/\Delta u_2$ ratio with β_f.

The previous results allow to suggest the following procedure for improved CPT interpretation: (a) combined standard Δu measurements can be used to estimate the relative fluid-soil skeleton stiffness, with the results in Fig. 7; and (ii) the latter can be adopted to infer a convenient value of N^*_{kt} (Fig. 4), to be used in the derivation of a reliable value of undrained strength.

In case the stiffness of the soil skeleton was known, typically from laboratory tests, the results in Fig. 7 could be replotted as a relationship between $\Delta u_1 / \Delta u_2$ and β_f (Fig. 8).

In this case, multiple CPTu measurements taken at different times (ideally in different seasons) from the same location would allow to exploit $\Delta u_1 / \Delta u_2$ to evaluate the seasonal variation of both gas development and undrained shear strength.

4 Conclusions

In organic soft soils, the formation of gas due to the biological degradation of the organic matter poses challenges in interpreting cone penetration test results. Misinterpreting these results may lead to either overestimation or underestimation of the undrained shear strength, which impacts on both geotechnical design and assessment.

The results of the numerical study open a new perspective on the dependence of the CPT measurements on the fluid compressibility and help in providing a theoretical justification for the high variability often seen in empirically derived cone factor values for organic clays.

Given that the gas volume fraction depends on atmospheric pressure and temperature, the CPTu readings and cone factor values used to estimate the undrained shear strength will vary across seasons. The relationship between undrained shear strength and cone factor with the relative fluid-soil stiffness ratio was explored. The findings suggest that pore pressure measurements taken at the cone tip and at the shoulder can serve as a valuable tool to estimate both the percentage of gas pockets within the soil and the cone factor value.

The financial support of the Dutch Organisation for Scientific Research (NWO) to the projects "Sustainable Dykes" (TWM.BL.019.010) is gratefully acknowledged. Data used are available from the corresponding author by request.

References

1. P. K. Robertson & K. L Cabal, Guide to Cone Penetration Testing for Geotechnical Engineering. (Gregg Drilling & Testing, Signal Hill, CA, 2015).
2. C. I. Teh, G. T. Houlsby, An analytical study of the cone penetration test in clay. Géotechnique **41**, 17–34 (1991).
3. T. Lunne, P. K. Robertson, J. M. Powell, Cone Penetration Testing in Geotechnical Practice. (Blackie Academic & Professional, London, UK, 1997).
4. P. W. Mayne, J. Peuchen, Evaluation of CPTU Nkt cone factor for undrained strength of clays. in Cone Penetration Testing 423–429 (2018).
5. H.E. Low, T. Lunne, K.H. Andersen, M.A. Sjursen, X. Li, M.F. Randolph, Estimation of intact and remoulded undrained shear strengths from penetration tests in soft clays. Géotechnique **60**, 843–859 (2010).
6. S. J. Wheeler, The undrained shear strength of soils containing large gas bubbles. Géotechnique **38**, 399–413 (1988).
7. Y. Hong., L. Wang, C. Ng, B. Yang, Effect of initial pore pressure on undrained shear behaviour of fine-grained gassy soil. Canadian Geotechnical Journal **54**, 1592–1600 (2017).
8. C. Jommi, S. Muraro, E. Trivellato, C. Zwanenburg, Experimental results on the influence of gas on the mechanical response of peats. Géotechnique **69**, 753–766 (2019).

9. H. F. Zhao, S. Muraro, C. Jommi, Gas exsolution and gas invasion in peat: towards a comprehensive modelling framework. Géotechnique Letters **10**, 461–467 (2020).
10. D. Tarragó, A. Gens, Gas Effect On CPTu and Dissipation Test Carried Out On Natural Soft Soil of Barcelona Port. in Cone Penetration Testing 2018 605–609 (CRC Press, 2018).
11. L. Mele, P. Bonassisa, S. Lirer, A. Flora Induced Partial Saturation as mitigation technique against liquefaction: an energetic approach for design tools. Japanese Geotechnical Society Special Publication **10**, 1677–1683 (2024).
12. H. Wang et al. Study on the CPTu inversion methods for strength and consolidation parameters of gassy soil with different gas contents. Applied Ocean Research **146**, 103960 (2024).
13. A. Halleux, K. Boschi, L. Flessati, C. Jommi, G-PFEM-aided derivation of undrained shear strength of organic clays from CPT data. in Proceedings of the 7th International Conference on Geotechnical and Geophysical Site Characterization 1896–1902 (2024).
14. C. Jommi, S. Muraro, C. Chao, Interpreting repeated CPT in unsaturated soils. in 7th International Conference on Geotechnical and Geophysical Site Characterization (CIMNE, 2024).
15. M. A. Mánica, M. Arroyo, A. Gens, L. Monforte, Application of a critical state model to the Merriespruit tailings dam failure. Proceedings of the Institution of Civil Engineers – Geotechnical Engineering (2022).
16. K. Boschi, M. Arroyo, L. Monforte, J. M. Carbonell, A. Gens, Coupled hydromechanical modelling of cone penetration in layered liquefiable soils. Geotechnique **75**, 308–322 (2024).
17. H. S. Yu, CASM: A unified state parameter model for clay and sand. Int. J. Numer. Anal. Methods Geomech. **22**, 621–653 (1998).
18. E. Ponzoni, Historical constructions on natural silty soils accounting for the interaction with the atmosphere. (Università degli Studi di Brescia, 2017).
19. S. Muraro, The deviatoric behaviour of peat: a route between past empiricism and future perspectives. (Delft University of Technology, 2019).
20. S. Pietruszczak, G. N. Pande, On the mechanics of partially saturated soils. Comput. Geotech. **12**, 55–71 (1991).
21. K. A. Schmidt, G. K. Folas, B. Kvamme, Calculation of the interfacial tension of the methane–water system with the linear gradient theory. Fluid Phase Equilibria **261**, 230–237 (2007).
22. L. Monforte, M. Arroyo, J. M. Carbonell, A. Gens, Numerical simulation of undrained insertion problems in geotechnical engineering with the particle finite element method (PFEM). Comput. Geotech. **82**, 44–156 (2017).
23. L. Monforte, M. Arroyo, J. M. Carbonell, A. Gens, Coupled effective stress analysis of insertion problems in geotechnics with the particle finite element method. Comput. Geotech. **101**, 114–129 (2018).
24. P. Dadvand, R. Rossi, E. Oñate, An object-oriented environment for developing finite element codes for multidisciplinary applications. Archives of Computational Methods in Engineering **17**, 253–297 (2010).
25. L. Monforte, M.O. Ciantia, J. M. Carbonell, M. Arroyo, A. Gens, A stable mesh-independent approach for numerical modelling of structured soils at large strains. Comput. Geotech. **116**, 103215 (2019).